Article

The Steady Wake of a Wall-Mounted Rectangular Prism with a Large-Depth-Ratio at Low Reynolds Numbers

Arash Zargar [1,†], **Ali Tarokh** [1,2,†] and **Arman Hemmati** [1,*,†]

1 Department of Mechanical Engineering, University of Alberta, Edmonton, AB T6G 1H9, Canada; zargar@ualberta.ca (A.Z.); atarokh@lakeheadu.ca (A.T.)
2 Department of Mechanical Engineering, Lakehead University, Thunder Bay, ON P7B 5E1, Canada
* Correspondence: arman.hemmati@ualberta.ca; Tel.: +1-780-492-1672
† These authors contributed equally to this work.

Abstract: The wakes of wall-mounted small (square) and large (long) depth-ratio rectangular prisms are numerically studied at Reynolds numbers of 50–250. The large depth-ratio significantly alters the dominance of lateral secondary flow (upwash and downwash) in the wake due to the reattachment of leading-edge separated flow on the surfaces of the prism. This changes the wake topology by varying the entrained flow in the wake region and changing the distribution of vorticity. Thus, the magnitude of vorticity significantly decreases by increasing the prism depth-ratio. Furthermore, the length of the recirculation region and the orientation of near wake flow structures are altered for the larger depth-ratio prism compared to the square prism. Drag and lift coefficients are also affected due to the change of pressure distributions on the rear face of the prism and surface friction force. This behavior is consistently observed for the entire range of Reynolds numbers considered here. The wake size is scaled with $Re^{1/2}$, whereas drag coefficient scaled with $Re^{-0.3}$.

Keywords: wake dynamics; DNS; wall mounted; prism; CFD; heat exchange; depth ratio

1. Introduction

The flow structures around wall-mounted rectangular cylinders or prisms have been extensively studied in the literature, partly due to their broad engineering applications and partly because of their complex dynamics. Particularly at low Reynolds numbers, understanding the wake of a wall-mounted long prism has major implications in improving the design of electronic chips for better cooling, biomedical devices, vortex generators, pipe roughness elements, and small heat exchangers [1]. In these applications, the detail understanding of the flow field around the prism is critical in optimizing the design and performance of various devices, for example fast response accurate measuring equipments such as hotwire. Recent developments have revealed that existing experimental and numerical studies do not provide a thorough description of the flow field in the detached flow regions of the prism [2], although flow structures around small depth-ratio (tall) prisms are highly organized [3]. Here, the prism dimensions are normalized by the prism aspect ratio, defined as $AR = h/w$, and depth ratio, defined as $DR = l/h$ (see Figure 1).

Wake models have been developed for the flow around wall-mounted circular cylinders, which date back to the work of Taneda (1952) [4]. Since then, there have been several modifications and upgrades to these models based on the cylinder characteristics and flow field conditions, a summary of which is provided by Sumner (2013) [5]. Wang et al. (2004) [6] proposed a comprehensive model for the wake of a wall-mounted rectangular cylinder. In this model [6], they classified the wake vortices of a wall-mounted cylinder into four different structures. There are tip and base vortices formed in the wake, which coincide with the formation of downwash and upwash flow. The spanwise vortices are Kármán type structures in the middle height of the body, and the horseshoe vortex is formed in front of the body and continue to the wake region. Later on Wang et al. (2009) [3]

modified this model base on their detailed experimental study of the near wake region immediately behind the cylinder. This study revealed the presence of a single arc-like structure within the near wake region. They argued that spanwise, tip and base vortices are inherently connected and form an arch-type structure regardless of the aspect ratio of the cylinder. They also reported that both asymmetric and symmetric vortex shedding is observed simultaneously, but the probability of an asymmetrically arranged vortices is higher at the middle height of the object.
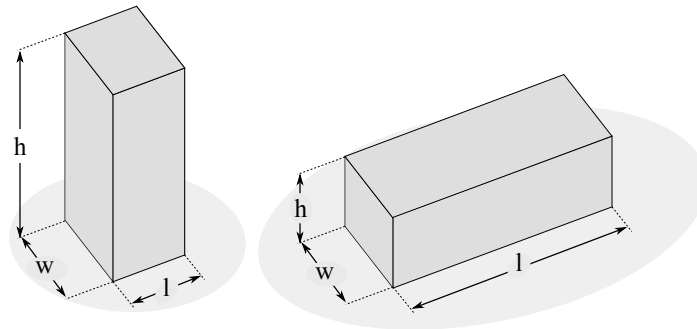

Figure 1. Schematics of the dimensions of short-depth-ratio (**left**) and large-depth-ratio (**right**) prisms.

Most recently, da Silva et al. (2020) [7] identified multiple mean wake structures, instead of a single arc-type structure, formed around a wall-mounted square cylinder (small depth-ratio prism) with $AR = 3$ at $Re = 500$. As shown in Figure 2, it was suggested that these structures have different origins, contrary to the models discussed by Wang et al. (2009) [3]. Particularly, da Silva et al. (2020) [7] showed that the structures on the upper surface of the cylinder appear to fade, while wake tip vortices are formed because of three-dimensional deflection of the separated flow from the side leading edges of the cylinder. Moreover, there is a spanwise vortex structure named "B_t" that is formed by the folding of the separated shear layer from the free end leading edge of the cylinder. This newly identified structure has a different origin from the so-called legs of the arc-type structures. da Silva et al. (2020) [7] identified that the differences observed compared to the wake model of Wang et al. (2009) [3] may be attributed to the transitional nature of the latter wake compared to the mean wake considered in the lower Reynolds number study. These studies, although limited to small depth-ratios, have revealed that, depending on the cylinder aspect ratio and Reynolds number, there are multiple structures formed in the wake with distinct characteristics.
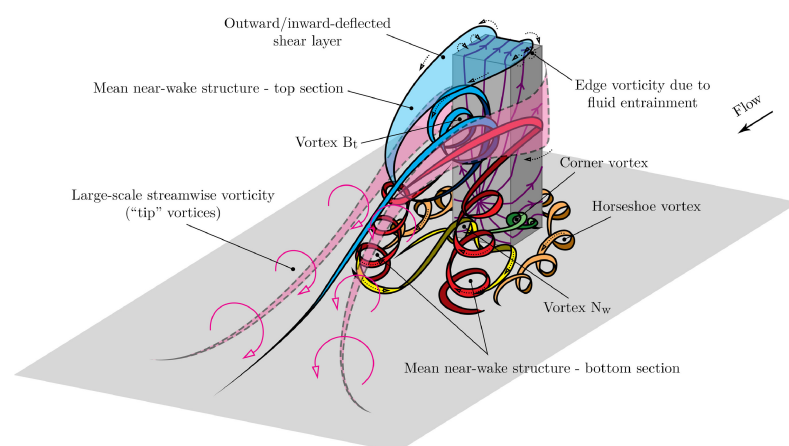

Figure 2. The time averaged wake model for a wall-mounted square cylinder from da Silva et al. (2020) [7].

Wei et al. (2001) [8] visualized the effect of increasing Reynolds number, defined as $Re = hU_\infty/\nu$, where h is the prism height, U_∞ is freestream velocity, and ν is the fluid kinematic viscosity, on the horseshoe vortex structure in front of a wall-mounted cylinder. They showed that increasing Reynolds number can make the horseshoe vortices oscillatory. Furthermore, these oscillations have a significant impact on the upstream velocity fluctuations. Zhang et al. (2017) [9] conducted Direct Numerical Simulations (DNS) at different Reynolds numbers and found that changing the Reynolds number can change the types of flow structures behind the wall-mounted square cylinder. They identified a new type of transitional flow structure, namely "Six-Vortices," in addition to dipole and quadrupole structures. Using DNS, Rastan et al. (2017) [1] classified the wake regimes of a short-depth (vertically oriented) cylinder with $AR = 7$ into five different regimes: steady flow ($Re < 75$), transition to unsteady flow ($75 < Re < 85$), laminar flow ($85 < Re < 150$), transition to turbulent flow ($150 < Re < 200$) and turbulent flow ($Re > 200$). They determined that the wake is characterized by dipole structures at $Re < 85$, whereas quadrupole structures dominate the wake at $Re > 150$. At $85 < Re < 150$ the wake is dominated by other structures that transition the wake into what is called Hexapole state. The presence of extra vortices in Hexapole wakes is attributed to the bending of streamlines at the lower part of the cylinder. These studies provided a detailed description of the wake of small depth ratio cylinders, while the effect of large depth ratios is unknown.

The cross-sectional shape of a wall-mounted geometry is known to influence the flow separation, and thus, the wake. For example, Uffinger et al. (2013) [10] investigated the effect of cross-sectional shape of a wall-mounted geometry (i.e., square cylinder, cylinder with elliptical after body, and cylinder with wedge in front) on its wake using both numerical and experimental methods at $Re = 1.28 \times 10^4$. They determined that cross-sectional shape of the prism (cylinder) affects the strength of the interaction between the flow over the top of the body and the Kármán type vortices along its sides. Other similar studies on circular and rectangular cylinders (e.g., Sattari et al., 2012 [11] and Rastan et al., 2017 [1]) further expanded on this observation at $Re = O(10^4)$. Joubert et al. (2015) [12] investigated the flow field of a wall-mounted cylinder with the length to width ratio of 2.63 and the aspect ratio of 5 at Reynolds number of $Re = 7.6 \times 10^4$. They reported that the flow reattachment on the upper surface is one of the main flow changes by increasing the length of the cylinder. Lim et al. (2015) [13] investigated the effect of depth-ratio ($0.5 \leq DR \leq 2$) and prism incidence angle ($0° \leq i \leq 45°$) at Reynolds number of $Re = 4.6 \times 10^4$ using experimental and numerical methods. They reported that changing the depth-ratio and incidence angle parameters lead to a strong variation of flow field vortex structures and surface pressure on the prisms. Therefore, analyzing these parameters for designing new engineering applications is critical. Wang et al. (2019) [14] experimentally investigated the effect of aspect ratio and depth ratio on the flow field of rectangular cylinders at the range of Reynolds numbers of 0.78×10^4–2.33×10^4. They reported that increasing aspect ratio changes the flow structures from dipole to quadrupole vortex arrangement. However, changing the depth ratio does not significantly change the flow structures unless it leads to flow reattachment on the side surfaces.

The prism aspect ratio is another geometrical parameter that has substantial effect on the wake dynamics [15,16]. Using DNS, Saha (2013) [15] illustrated that the strength of tip downwash flow, drag coefficient, Strouhal number, and wake flow unsteadiness of a short-depth (vertically oriented) cylinder increases with increasing aspect ratio at $Re = 250$. Later experimental studies of Sumner et al. (2017) [16] focused on a higher Reynolds number of 4.2×10^4, which identified the presence of a critical aspect-ratio, after which the wake regime is altered. However, these studies focused on high Re and small depth-ratios. Rastan et al. (2019) [17] explained the effect of changing aspect ratio on the wake flow structures of a wall-mounted cylinder at Reynolds number of $Re = 250$. They classified different streamwise flow structures and mentioned that at $AR = 7$, the legs of the arc type structure form with the staggered arrangement, and the vortex shedding is irregular. However, the arrangement of the arc-type structure legs and vortex shedding is regular for

the case of $AR = 2$. Furthermore, the occurrence of both of these conditions are captured in the wake of a rectangular cylinder with aspect ratio of $AR = 4$.

The boundary layer thickness [18,19] and incident angles [20] are also known to effect the wake dynamics at higher Reynolds numbers. With respect to the former, for example, the experiments of Hosseini et al. (2013) [18] and El Hassan et al. (2015) [19] at $Re = 1.2 \times 10^4$ identified that the boundary layer has a profound effect on the wake structures and vortex dynamics, including changing the interaction of horseshoe vortices with structures in the wake. Although these were limited to higher Reynolds numbers, similar behavior is intuitively expected for lower Re flows. Behera et al. (2019) [21] investigated the effect of changing the boundary layer thickness on the flowfield of a square cylinder with an aspect ratio of 7 at Reynolds number of 250. They reported the simultaneous occurrence of the two modes of anti-symmetric and symmetric wake shedding processes regardless of the boundary thickness. Behera et al. (2019) [21] also mentioned that occurrence of the symmetric mode of shedding coincides with the strongest values of upwash and downwash flow. Zhou et al. (2013) [22] investigated the flow features of a two-dimensional rectangular prism with depth ratio of 5 in non-shear and shear incoming flow at Reynolds number of $Re = 2.2 \times 10^4$. They reported that the peak frequency of the drag and lift coefficients become identical in shear flow. Furthermore, the unstable separating and reattaching flows on the side faces of the prism at uniform flow appeared more stable.

The wake features of a wall-mounted prism (cylinder) have been investigated extensively in the literature with respect to the implications of aspect ratio, incidence angle, boundary layer thickness and Reynolds number. However, these studies almost entirely focused on short-depth-ratio cylinders at moderate and high Reynolds numbers. Thus, we aim to address this knowledge gap by extending the wake characterization for larger depth-ratio (longer) prisms. Therefore, the wake formed at low Reynolds number behind large depth-ratio wall-mounted prisms will be fully characterized with implications in design of vortex generators, small-scale heat exchanges, including electronic micro-chips, and roughness elements in pipes. Particularly related to the fundamentals of wake topology, studying the wake behind a large depth-ratio prism enables the evaluation of horseshoe vortex dynamics and its implications on the orthogonal flow behavior in the wake. In this study, the focus is on examining the wake of a large-depth-ratio (4.17) wall-mounted prism and compare it with that of a small depth-ratio prism (square cylinder) at low Reynolds numbers ($50 \leq Re \leq 250$). The main objective of this study is to establish the changes in the wake due to the larger depth-ratio of the prism. The paper structure follows a detailed description of the methodology and numerical setup in Section 2. The main results and discussions are included in Section 3 followed by the summary of conclusions in Section 4.

2. Methodology

This study considers the flow around short and long depth-ratio wall-mounted prisms at $Re = 50 - 250$. This range of Reynolds number is selected to best identify the changes associated with the large depth-ratio effects since the wake of the square prism at $Re = 250$ should be steady [15]. The prism dominant height (h) is used to normalize all dimensions and length-scales. For the long rectangular prism, the width is $w = 0.83$ h and the length (depth) is $l = 4.17$ h, which implies a depth-ratio of $DR = l/h = 4.17$. These dimensions were motivated by design of electronic chips and a particular flow manipulator for biomedical applications [23]. Moreover, this depth-ratio is larger than the critical aspect-ratio of 3–4 previously identified for infinitely span prisms [24]. The square prism has a width and length of $w = l = 0.83$ h, which translate to a depth-ratio of $DR = 0.83$. These dimensions are selected for the reference case, which satisfies the condition of $DR < 1$, and differs from the special case of a cube ($DR = 1$). The uniform inlet velocity corresponds to different Reynolds numbers based on the prism height (h). The boundary layer formed on the ground has a thickness of ≈ 0.5 h at the prism frontal face. The schematics of the long prism is shown in Figure 3. The prism cross-sectional area is in the yz-plane and it extends in the streamwise (x-) direction.
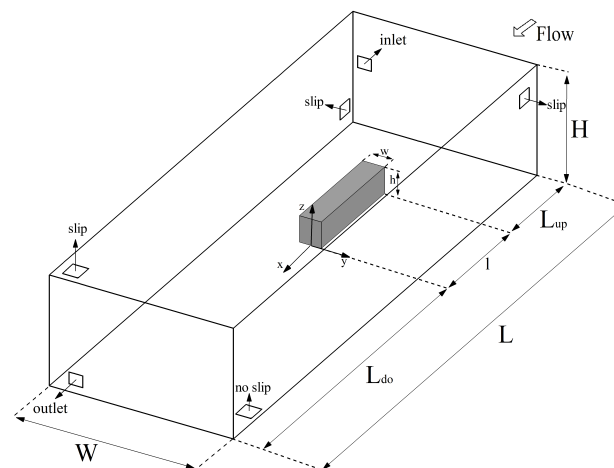
Figure 3. Schematic of the computational domain (not to scale).

2.1. Numerical Setup

The three-dimensional continuity (Equation (1)) and momentum (Equation (2)) equations are solved directly using OpenFOAM to examine the wake for both prisms:

$$\frac{\partial u_i}{\partial x_i} = 0,$$

(1)

$$\frac{\partial u_i}{\partial t} + \frac{\partial u_i u_j}{\partial x_j} = -\frac{1}{\rho}\frac{\partial p}{\partial x_i} + \nu\frac{\partial^2 u_j}{\partial x_i x_j},$$

(2)

where u_i and p are the velocity and pressure, respectively [25].

In the present study, the below definitions are considered for calculating the coefficients of drag, lift and pressure:

$$C_d = \frac{D}{0.5\rho U_\infty^2 A},$$

(3)

$$C_l = \frac{L}{0.5\rho U_\infty^2 A},$$

(4)

$$C_p = \frac{p - p_\infty}{0.5\rho U_\infty^2},$$

(5)

where D and L are the drag and lift forces, respectively, p is the fluid pressure, ρ is the fluid density, U_∞ is the free stream velocity, and A is the prism front face area.

The streamwise (x-), spanwise (y-), and normal (z-) dimensions of the computational domain, shown in Figure 3, are $L = 40\,h$, $H = 6\,h$, and $W = 16\,h$, respectively. The front face of the body is located $L_{up} = 10\,h$ from the inlet and $L_{do} = 25\,h$ from the outlet. The constant uniform velocity is applied as the inlet boundary condition. Sides and upper walls of the domain are set to slip boundary condition. The outlet boundary is set as the Neumann boundary condition ($\partial\phi/\partial n = 0$, where ϕ is any flow variable). The no-slip boundary condition is applied to the ground and body faces.

A non-homogeneous grid made of 4.5×10^6 and 3.9×10^6 hexahedral elements are used for the long and short rectangular prisms at $Re = 250$, respectively. To ensure that the effect of the Reynolds number will be identified thoroughly, the same mesh is utilized for lower Reynolds numbers. The spatial grid distribution for the long prism is shown in Figure 4. The grids are designed so that the maximum value of n^+ is below 0.55 at the walls at $Re = 250$, which enables capturing flow fluctuations associated with separated flow. The long prism domain edges contain 241 elements in the x-direction, 173 elements in the y-direction and 109 elements in the z-direction. Similarly, the short

prism contains $206 \times 173 \times 109$ elements along the $x \times y \times z$ directions, respectively. The timestep was set as 2.08×10^{-3} h/U_0 for the long and short prisms, which ensured that the maximum CFL number remained below 0.8 in the wake region with the most spatially refined grid. The spatial and temporal discretization of the governing equations are second-order accurate. Temporal discretization is based on second order accurate backward Euler method, and the discretization scheme of the gradient, divergence, and Laplacian terms are based on the second order Gauss Linear method. The residual momentum root-mean-square of 10^{-6} was set as the criteria for convergence for each timestep. The PIMPLE algorithm, which is a combination of Pressure Implicit with Splitting of Operator (PISO) and Semi-Implicit Method for Pressure-Linked Equations (SIMPLE) methods, is used for coupling the pressure and velocity fields. The computational domain for each case is divided into 16 separate regions for parallel computing. The simulations are completed using Intel Platinum 8160 F Skylake 2.1 GHz cores at 15,000 core hours.
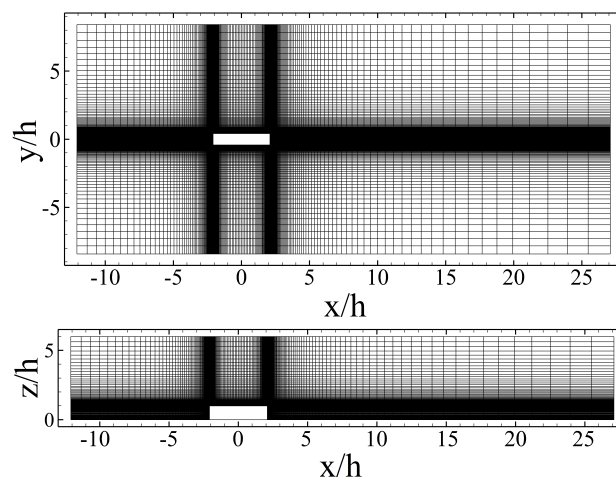

Figure 4. The spatial grid distribution for the long prism at $Re = 250$. Top view at $z/h = 0.5$ (**top**) and side view at $y/h = 0$ (**bottom**).

2.2. Verification and Validation of Results

The domain size is known to affect numerical results, and so does the spatial grid quality [26]. To address the former, the computational domain was designed such that its size exceeds those of Shah et al. (1997) [27], Krajnovic et al. (1999) [28] and Yakhot et al. (2006) [29] for a single cube, and Krajnovic et al. (2005) [30,31] for an Ahmed body. Furthermore, the sensitivity study on the computational domain size was based on three domains for the long prism. The grid quality analysis was carried out using three grids for the long prism as well. More details on these sensitivity studies can be found in Zargar et al. (2020) [32]. Here, only a summary of the verification and validation studies are provided for brevity. Table 1 shows the comparison of the grid quality in the current study with other similar studies of the flow around a rectangular prism or an Ahmed body model. The streamwise velocity profile calculated at a constant distance from the prism rear face is presented in Figure 5, which illustrates that the difference between Grid 2 and Grid 3 is less than 1%. The grid-quality sensitivity analysis indicated that Grid 3, which is the mesh used in the current study, is sufficient for capturing the main global flow features.

In an effort to validate the simulations in the absence of experimental data for this specific case, a similar "validation case study" was completed based on a square prism of aspect ratio 4 to compare with the DNS results of Saha (2013) [15] and Zhang et al. (2017) [9]. The calculated drag coefficient for the validation case is equal to $\overline{C_d} = 1.223$, which is very close the reported value of $\overline{C_d} = 1.23$ by saha (2013) [15]. Furthermore, as shown in Figure 6 and , the profile of stramwise and spanwise velocity collapse well with the result of Saha (2013) [15] and Zhang et al. (2017) [9] with small discrepancies. To further analyze the validity of the results, Figure 7 compares the numerically computed boundary layer in the

present study calculated at $x/h = -2.1$ and $y/h = -7$ with the analytically determined Blasius boundary layer solution. The good agreement between these results indicates that the simulations are adequate in capturing the main flow features.

Table 1. Numerical setup comparison between current and previous studies. n is the number of elements. The bold case is used for the simulations.

|	Method	Body Shape	*Re*	n	y_{max}^{+}
Grid 1	DNS	Rectangular prism	2.5×10^2	$190 \times 133 \times 86$	1.3
Grid 2	DNS	Rectangular prism	2.5×10^2	$210 \times 142 \times 93$	0.9
Grid 3 (Current Study)	DNS	Rectangular prism	2.5×10^2	$241 \times 173 \times 109$	0.55
Krajnovic et al. (1999)	LES	Cube (2D)	4.0×10^4	$64 \times 64 \times 64$	1.1
Yakhot et al. (2006)	DNS	Cube	5.6×10^3	$181 \times 121 \times 256$	0.76–6.46
Krajnovic et al. (2005)	LES	Ahmed body	2.0×10^5	1.65×10^7	0.33
Saeedi et al. (2016)	LES	Square Prism	1.2×10^4	$480 \times 160 \times 200$	0.59
Zhang et al. (2017)	DNS	Square Prism	$\leq 10^3$	$\leq 303 \times 228 \times 202$	–
Rastan et al. (2017)	DNS	Square Prism	$\leq 2.5 \times 10^2$	$203 \times 210 \times 154$	–
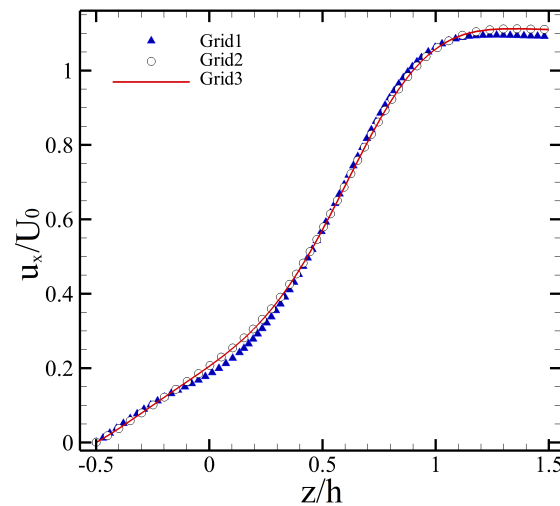
Figure 5. Grid sensitivity study based on streamwise velocity profile at $x/h = 3$ and $y/h = 0$ for the long prism.
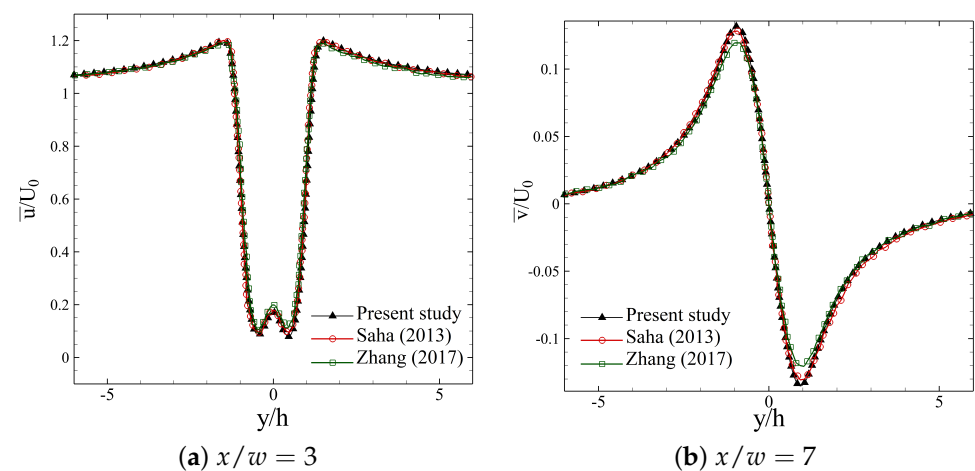

(**a**) $x/w = 3$
(**b**) $x/w = 7$

Figure 6. Time-averaged (**a**) streamwise and (**b**) spanwise velocity distributions at $Re = 250$ behind a rectangular prism with $AR = 4$ at $z/w = 3.5$ compared with DNS results of Saha (2013) [15] and Zhang et al. (2017) [9].
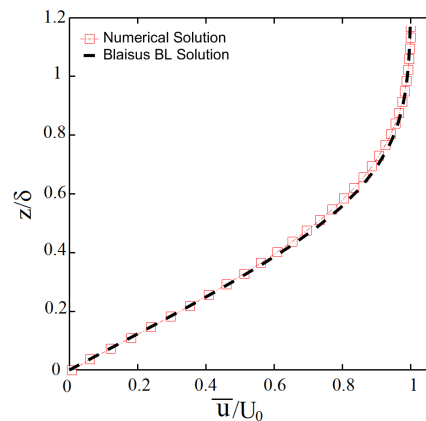
Figure 7. Profiles of time-averaged streamwise velocity profile inside the boundary layer for the long prism at $x/h = -2.1$ and $y/h = -7$, compared to the Blasius Boundary layer solution.

3. Results

This study focuses mainly on characterizing the wake of a large depth-ratio prism at the highest Re considered here, while comparing the wake topology to well-established wake of small depth-ratio (square) prisms. The longer surfaces of the long prism is expected to motivate reattachment of the shear layer formed on the leading edges of the prism. This hints at potentially major alternations to the wake. To begin, we look at the integral flow parameters, such as the coefficients of drag and lift, defined as forces acting in the positive x- and z-directions respectively, at $Re = 250$. The results showed that drag and lift coefficients are altered by the larger depth-ratio of the rectangular prims compared to the square prism. As shown in Table 2, the drag coefficient increases from $\overline{C_d} = 0.84$ for the square prism to 1.05 for the long prism. To find the source of this change, the distribution of pressure on the front and rear faces of the prisms are depicted in Figure 8. As expected, the pressure distribution on the front face of both prisms are fairly similar since the freestream characteristics mostly dictate the pressure of the front stagnation region. Conversely, the pressure distribution on the rear face of the two prisms strongly differ, which hints that the wake flow characteristics vary between the two bodies. Magnitude of the pressure coefficient on the rear face of the long prism is larger than that of the square prism. Furthermore, Figure 9 presents the pressure distributions across the rear and frontal face of the prisms on the symmetry plane ($y/h = 0$). As shown, the pressure coefficient on the prisms' front face are identical for both cases, while pressure is larger on the back face of the large depth-ratio prism. This implies that the increase of drag observed for the longer prism does not relate to a larger pressure drop in the wake. Thus, the additional drag must intuitively relate to larger frictional forces on the side and upper faces of the long prism.

Table 2. Time-average coefficients of lift ($\overline{C_l}$) and drag ($\overline{C_d}$) and recirculation length ($\overline{L_r}$) for both prisms at $Re = 250$.

Cases	Depth-Ratio (*DR*)	$\overline{C_l}$	$\overline{C_d}$	$\overline{L_r}$
Long Prism	4.17	0.24	1.05	2.2 h
Square Prism	0.83	0.31	0.84	2.4 h

To characterize the wake of a large depth-ratio (long) rectangular prism, the main wake features are thoroughly examined and compared with those of the square prism. The flow around a wall-mounted rectangular prism with an aspect ratio of 2.00 and $DR = 0.50$ at $Re = 250$ has been characterized as weakly unsteady by Saha (2013) [15]. However, the current results indicate that the flow around square ($DR = 1.00$ and $AR = 1.20$) and long ($DR = 4.17$ and $AR = 1.20$) rectangular prisms are steady at $Re = 250$. The velocity

and pressure are examined at 45 different points within the near and far wake of both prisms through time, which did not show even weakly unsteady characteristics. Furthermore, examining the instantaneous isosurface of the Q-criterion at different timesteps did not exhibit any temporal changes of wake flow structures. The flow steadiness can be attributed to the suppression of the Kármán type vortices by downwash and upwash flow created close to the top and bottom of the prisms, respectively. This agrees with observations reported in the literature (e.g., Sohankar, 2006 [33] and Saha, 2013 [15]) that decreasing the aspect ratio of a rectangular wall-mounted prism, for the case of the square prism, and increasing the depth ratio to such large values (>4), for the case of a long prism, have similar implications on eliminating the wake unsteadiness at low Reynolds numbers. A higher aspect-ratio square prism case was tested for validation, not shown here for brevity, which showed unsteadiness at $Re = 250$, similar to the observations of Saha (2013) [15].
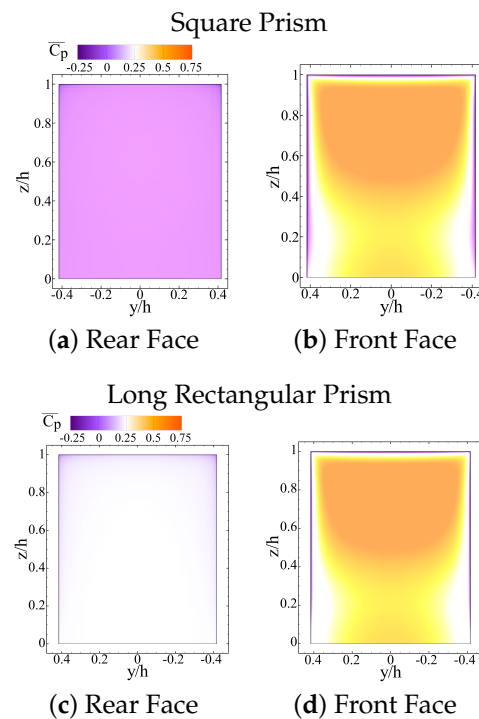

Figure 8. Distribution of $\overline{C_p}$ on the rear and front faces of the (**a**,**b**) square and (**c**,**d**) long prism.
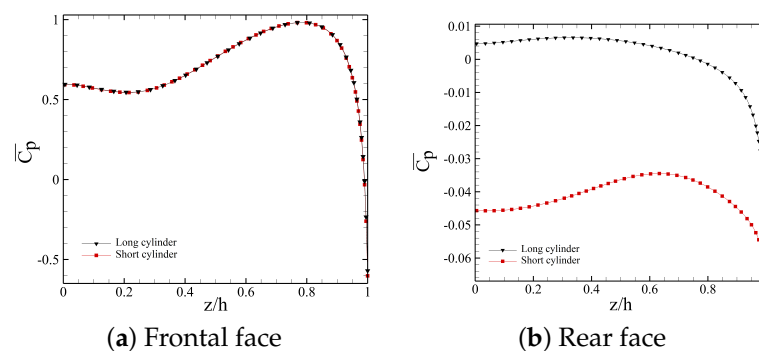

Figure 9. Profiles of surface pressure along the prism height at $y/h = 0$ for their frontal and rear faces.

Focusing on the flow field and main characteristics of the wake, the critical points on different faces of the long rectangular and square prisms are shown in Figures 10 and 11. The critical points are determined by streamlines of the velocity vector at the first cells from the walls. The nodal, saddle and focal points are identified as N, S, and F, respectively.

(**a**) Ground

(**b**) Rear face

(**c**) Front face

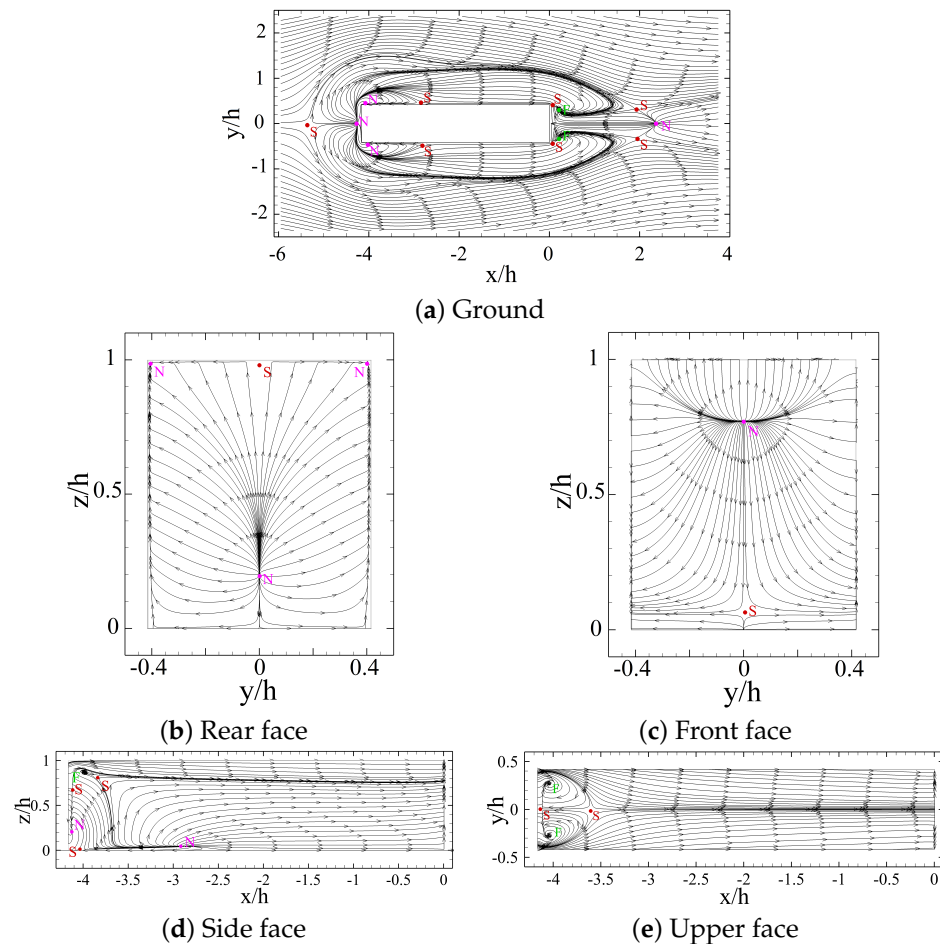(**d**) Side face

(**e**) Upper face

Figure 10. Critical points on the faces of the long prism.

Critical points are identified in the wake using streamlines on 2D planes both on and around the prisms. The total number of nodal, focal, and saddle points for the long prism are 14, 4, and 18, respectively. This agrees with the predictions of Tobak et al. (1982) [34], Chapman et al. (1991) [35] and Delery et al. (2013) [36]. According to them, there is a critical point theory for a wall mounted object, which also holds:

$$\Sigma(N + F) - \Sigma(S) = 0. \tag{6}$$

There is, however, a different wake topology expected for the square prism (short prism), in which case the result of Equation (6) is two instead of zero, according to Liakos et al. (2014) [37]. Based on the visualization of the critical points around the square prism in Figure 11, the total number of nodal, focal, and saddle points around the square prism are 13, 6 and 17, respectively. Thus, subtracting S from $N + F$ is equal to 2, which agrees with the findings of Liakos et al. (2014) [37]. It appears that two pairs of saddle points that are present on the side of the long prism (see Figure 10a) are merged in the case of the square prism. This leads to a decrease on the number of the saddle points compared to nodal points for the square prism, which indicates that Equation (6) can be different for a wall-mounted object based on the conditions of the study. Furthermore, there are some differences between the distribution of critical points on the wall-mounted cube in Liakos et al. (2014) [37] and the square wall-mounted prism in the current study. For example, they reported the presence of some saddle and nodal points on the edge between the front face and the ground close to the side face of the prism. However, these critical points are not observed for the square prism in the current study. These differences between the two cases are expected due to the differences in the geometries and thicknesses of the boundary layer. Moreover, comparing with Liakos et al. (2014) [37], the distribution

of critical points on the long prism at $Re = 250$ is similar to the distribution of critical points on a cube at $Re \geq 1000$. Looking at the results in Figures 10b and 11b, the nodal and saddle points on the rear face of the square prism (at $y/h = 0$) are formed farther from the ground compared to the long prism. This difference can be attributed to the more significant upwash flow in the wake of the square prism, which will be discussed later. It is also notable that there is not any saddle point on the upper rear face of the square prism. Alternatively, as shown in Figure 11e, there is a saddle point on the ending part of the upper face of the square prism, which indicates that there is a small region of reversed flow towards the trailing edge of the square prism upper face. Another significant difference of the distribution of critical points on faces of the short and long prism is that there exists an additional attachment nodal point and a saddle point behind the square prism in Figure 11a. The attachment nodal point is formed because of the interaction of the separated shear layer with the rear face of the prism. The saddle point is also the result of the interaction of the former nodal point and the last nodal point of the wake region.
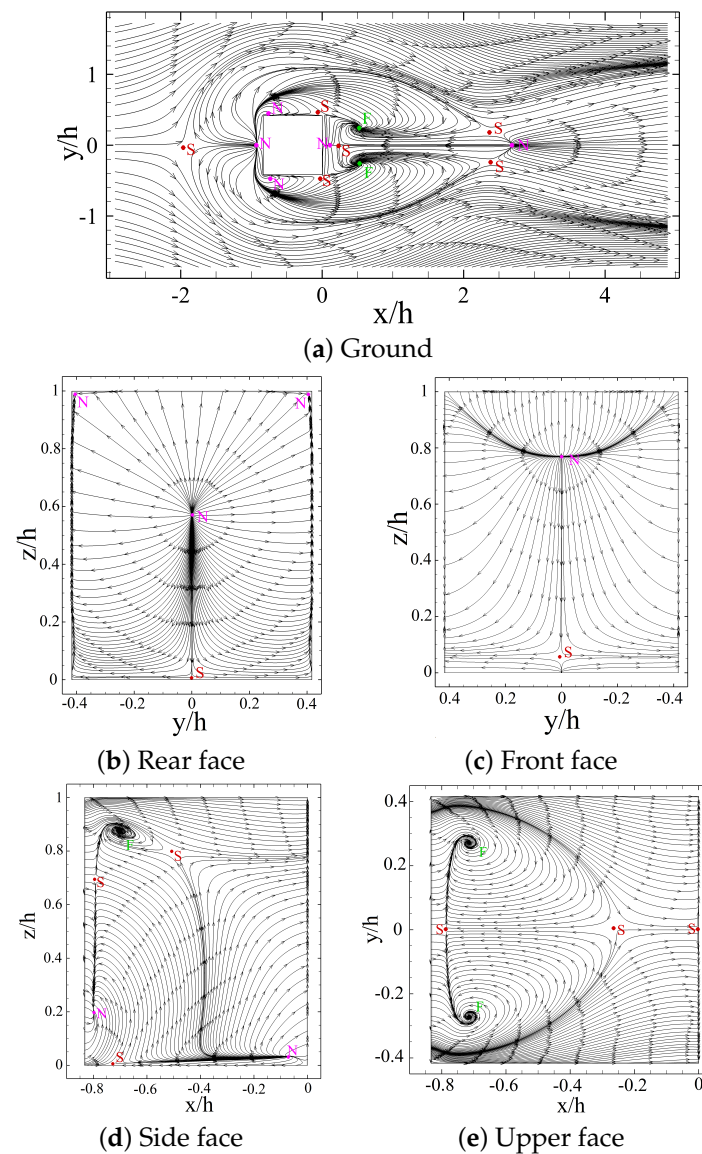

(**a**) Ground

(**b**) Rear face

(**c**) Front face

(**d**) Side face

(**e**) Upper face

Figure 11. Critical points on the faces of the square prism.

The iso-surface of the *Q*-criterion, normalized using the prism height (h) and freestream velocity (U_∞) and denoted by Q^*, are shown in Figures 12 and 13 from two perspectives: the front and rear views of the prism. The plots in Figure 13 identify that the separated

shear layer from the leading edge of the square prism is connected to the wake structures, which agrees with the existing models [3]. For the long prism, however, the structures are separated between the leading and trailing edge of the prism in Figure 12. Furthermore, the legs of the horseshoe vortex are extended into the wake and interact with the structure formed behind the square prism. This can directly impact the wake dynamics. Conversely, the wake structure of the long prism is located at a relatively long distance from the legs of the horseshoe vortex. The shorter depth of the square prism allows for interaction of the wake structures on the trailing edge of the prism, while the horseshoe vortex legs formed around the long prism are highly distorted and lack coherence at the trailing edge of the prism. Thus, there is no interactions between horseshoe structures and the wake behind the body. This differs from the square prism wake model.
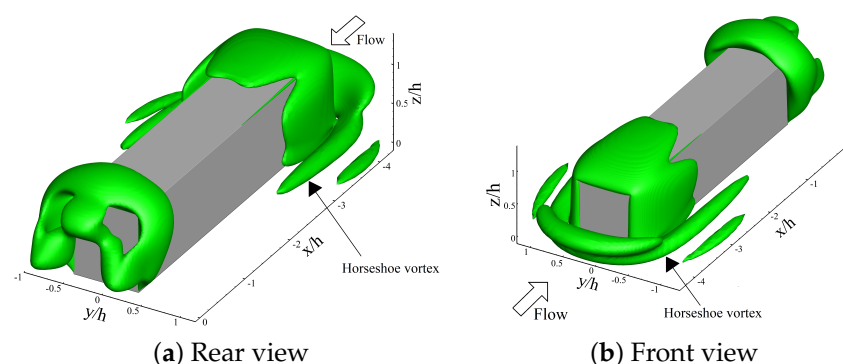

(**a**) Rear view　　　　　　　　　(**b**) Front view

Figure 12. The isosurface of $Q^* = 4.42 \times 10^{-2}$ in the wake of the long rectangular prism.

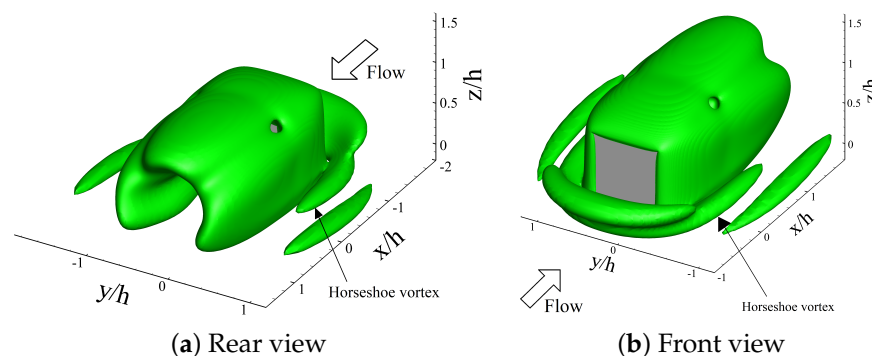(**a**) Rear view　　　　　　　　　(**b**) Front view

Figure 13. The isosurface of $Q^* = 4.42 \times 10^{-2}$ in the wake of the square prism.

The effect of large depth-ratio on upwash flow is apparent in Figure 14, where there is evidence of a strong upwash flow for the square prism and not the long prism. The upwash effect in the wake of the long prism is very narrow and limited to the vicinity of the prism rear face (see Figure 14a,b). This change in the wake behavior is associated with the change in interaction between the horseshoe vortex and the tip structure at the trailing of the prism. Moreover, this provide further evidence in comparison to the larger aspect ratio prisms, i.e., $AR = 2$ in Saha (2013) [15], that the height of the boundary layer at the prism rear face plays an essential role in the wake flow characteristics. Another critical difference between the two prisms is related to the downwash flow in the middle of the long prism, where there is a stronger downwash effect in the outer regions. This observation is also supported by the streamline plots on 2D planes of Figure 15. This implies that the entrainment of the freestream flow due to the separated shear layer increases the strength of the upwash and downwash flow. However, its effect on the upwash flow is more apparent near the symmetry plane, whereas its effect on the downwash is more evident close to the junction of the side and rear faces.
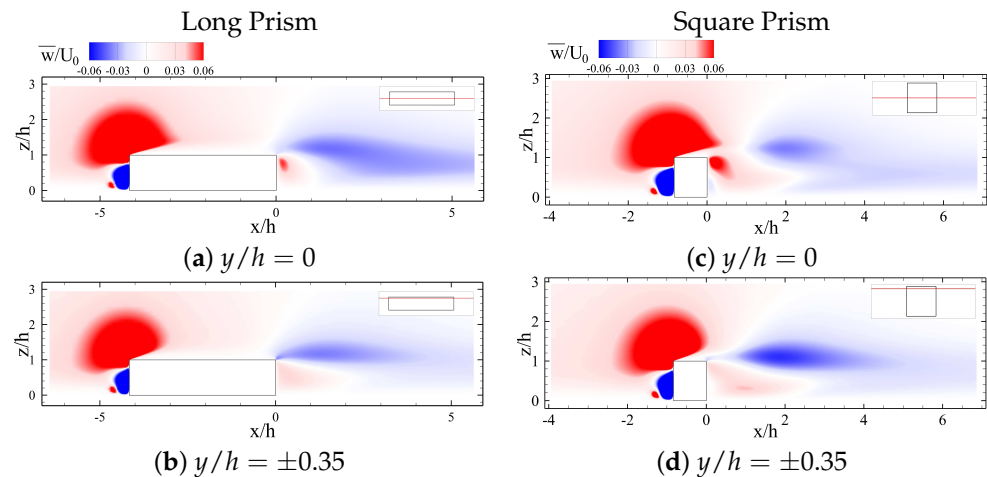
Figure 14. Contours of spanwise velocity at different planes along (**a**,**b**) the long prism and (**c**,**d**) the square prism. Red and blue regions correspond to upwash and downwash flow, respectively.
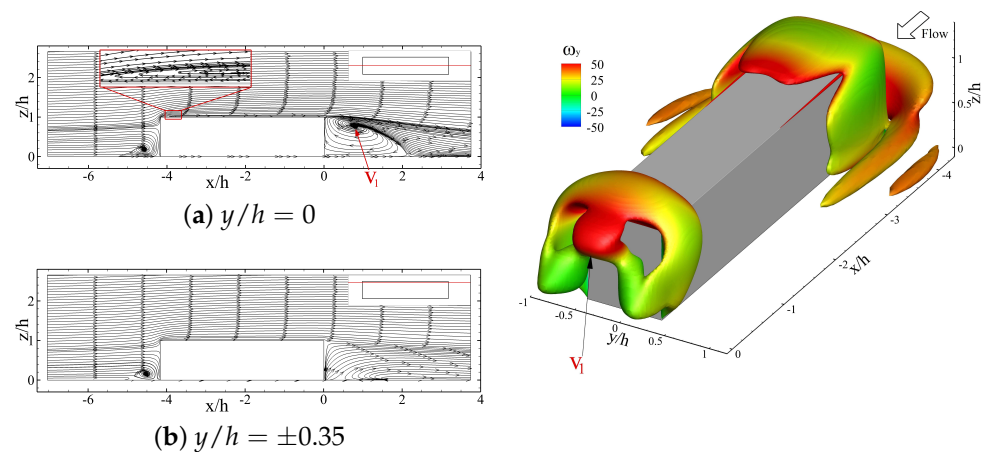

Figure 15. Isosurface of $Q^* = 4.42 \times 10^{-2}$ overlaid by the contour of y-component of vorticity and side view of the wake structure of the long prism.

As shown in Figures 15 and 16, the cross-flow in the wake is symmetric for both prisms. However, the presence of the boundary layer effects along the z-direction leads to a strongly antisymmetric wake in the normal (z-) direction. In the normal mid-plane of the prism (middle plane in the z-direction), there are focal points that correspond to laminar vortical structures in the wake (see Figure 16b). It can be seen from the contours superimposed on the isosurface of Q-criterion (Figures 15 and 16) that the rotational motion of the wake structure at a lower height (close to the ground) and higher part of the long prism are restricted to the z- and y-directions, respectively. The interconnection of these structures, which is apparent from the combination of 2D (streamline and contours) and 3D (iso-surface) visualizations, implies that their behavior is within a single structure that deforms and diffuses in the wake. The separation bubble close to the leading edge of the body is highlighted in Figure 15a, on the mid-plane of the prism, which does not extend into the outer wake. This implies that the reattachment on the prism upper face is stationary and it does not contribute to the tip structure typically formed on the prism rear, as per the model of Wang et al. (2009) [3]. There also exists the same separation bubble on sides of the long prism (Figure 16b) as it was also observed on the top face of the prism in Figure 15a. The side-bubbles also appear on the mid-plane for the prism, similar to the top-face bubble. Comparing such behaviors to the wake of the square prism in Figures 17 and 18, there is a similarity in the formation of bubbles on top and side faces of the prism. However, there appears to be a larger laminar structure in the outer wake of the square prism, which leads to a large flow entrainment (downwash flow) compared to the long prism. The center of

the wake structure behind the square prism in Figure 17b is 0.5 h farther away from the rear face of the prism compared to the long prism in Figure 15a.
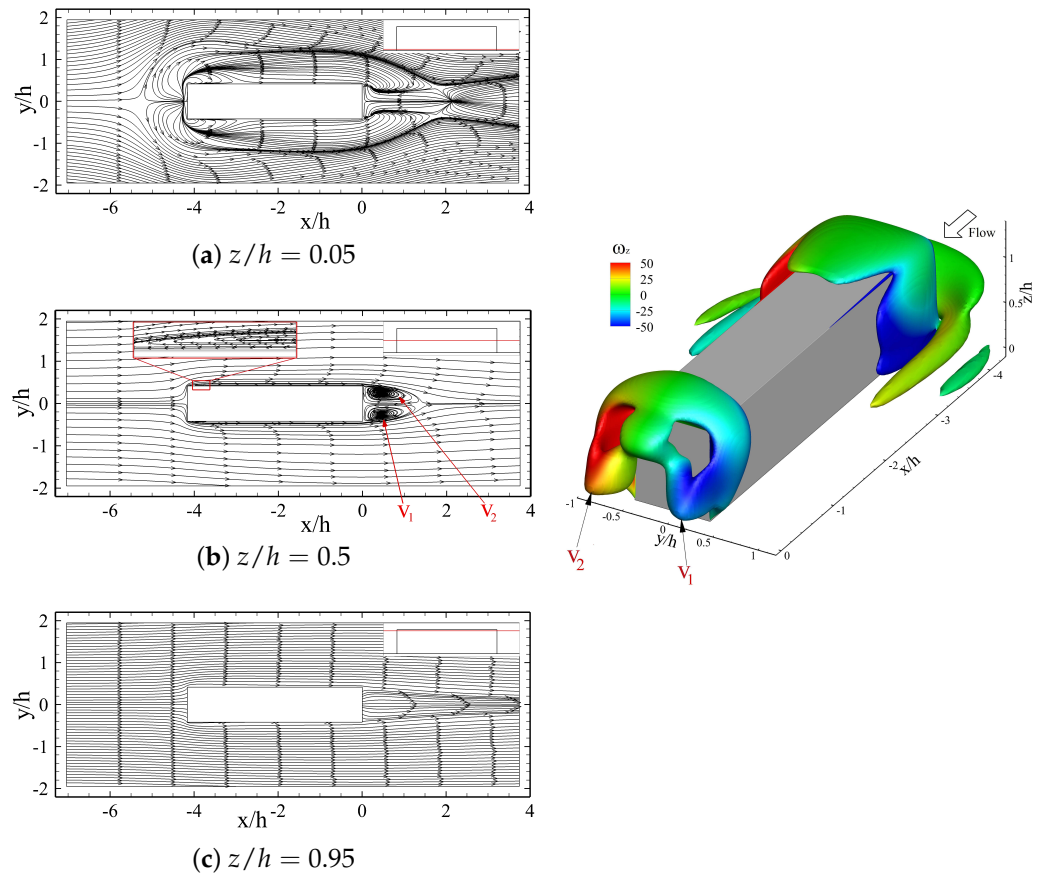

(**a**) $z/h = 0.05$

(**b**) $z/h = 0.5$

(**c**) $z/h = 0.95$

Figure 16. Isosurface of $Q^* = 4.42 \times 10^{-2}$ overlaid by the contour of z-component of vorticity and top view of the wake structure for the long prism.
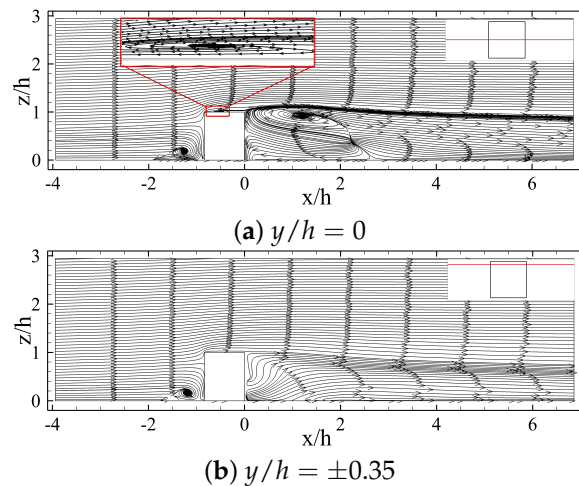

(**a**) $y/h = 0$

(**b**) $y/h = \pm 0.35$

Figure 17. The side (xz-plane) view of the wake structure of the square prism.

The streamline plots of Figure 18b identify a larger streamline curvature angle of 18.4° in the shear layer of the square prism compared to the long prism, where the curvature angle is 10.9° in Figure 16. The curvature angles are measured close to the mid-height plane at $y/h = 0.3$ using $\alpha = \tan^{-1}(v/u)$, where α is the streamline angle of curvature. The smaller α for the long prism implies that there is not a significant flow entrainment into the immediate wake [38]. This wake behavior appears very different for the square

prism in Figure 18a. Here, there is a significantly larger streamline curvature, due to the shorter depth of the prism, which implies a stronger freestream flow entrainment in the wake region. Streamline of the long and square prisms shows that the length and height of the wake region of the square prism are greater than the long prism. Particularly, the vortices formed in the wake of the square prism extend up to 2 h downstream in the wake, whereas the extension of these structure for the long prism is reduced by a factor of 2 (see Figures 15a, 16b, 17a and 18b). This trend persists across the flow field in the spanwise (*y*-) and normal (*z*-) directions. The vortex structure in *z*-direction in the middle region of the square prism extends to the upper regions, whereas it was constrained to the mid-plane of the longer prism. This structure for the long prism is completely different in the middle and upper regions. This indicates that the extension of the flow structures in the spanwise direction is inherently related to the strength of the upwash flow. The separation bubble close to the leading edge of the body is highlighted on the middle planes (see Figures 17a and 18b). This separation bubble does not extend to the outer regions. Furthermore, the length of this structure is not affected by changing the depth ratio. Despite this similarity, there exists a tip structure in the wake, which follows a different dynamics for long prisms compared to shorter prisms at low *Re*. It appears that the wake of the square prism is dominated by the downwash flow induced by larger (in apparent size) and stronger (in vorticity magnitude) trailing structures, which interact with the horseshoe vortex in the immediate wake. However, the long prism involves a distinctly smaller (in apparent size) and weaker (in vorticity magnitude) structure formed at the trailing-edge of the prism that do not interact with the boundary layer. Thus, the flow appears steady in the wake.
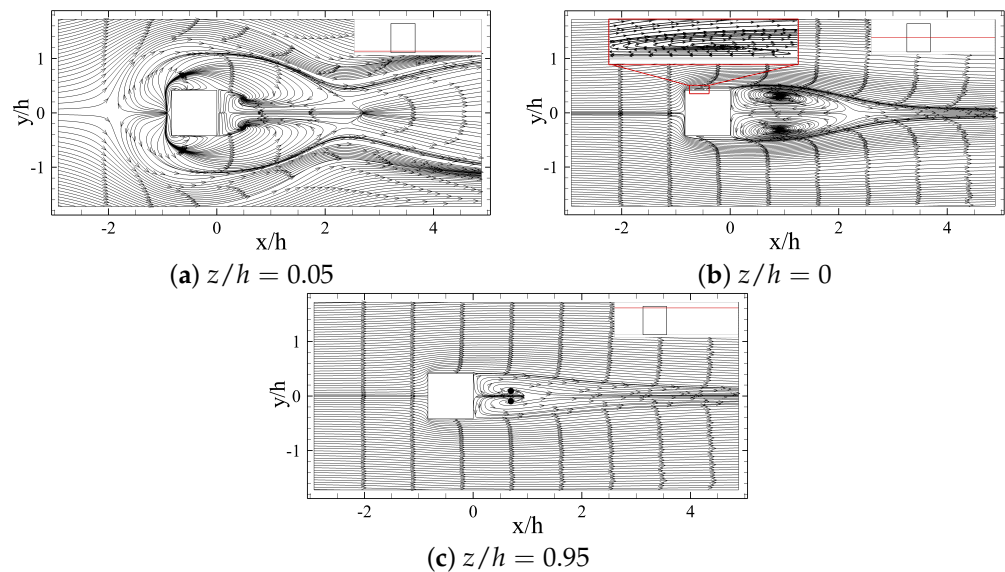

(**a**) $z/h = 0.05$

(**b**) $z/h = 0$

(**c**) $z/h = 0.95$

Figure 18. The top (*xy*-plane) view of the wake structure of the square prism.

Figure 19 shows the vorticity contours in the near wake region of the prisms. The larger magnitudes of spanwise and streamwise components of vorticity in the wake region of the square prism can lead to larger streamline curvatures. This provides further evidence of the stronger entrainment in the wake of the square prism compared to the long prism. The separated shear layer from the leading edge exhibits a large vorticity magnitude for both prisms. In the case of the square prism, the leading edge separated flow impacts the wake structures through what can be described as flow entrainment. However for the long prism, the reattachment of the flow on the upper and side faces prevents any entrainment mechanism. The presence of counter-rotating vortices in two sides of the prism implies that Kármán type vortices are suppressed by the upwash and downwash flow in both cases, due to the small aspect ratio of the prisms.

For a better understanding of the vortex structures around the body, two-dimensional streamlines along different planes perpendicular to the streamwise direction (cross-sectional planes) are shown in Figure 20. Two counter-rotating vortical structures are observed behind the long prism, which expand by moving farther away from the body. Since the rotational direction of these structures creates a downwash flow in the mid plane region ($y/h = 0$), to follow the existing definitions for tip vortex structure [1], these vortices should be tip vortices. Thus, it seems that the small aspect-ratio of the considered prisms leads to the elimination of the streamwise base vortices in the wake region, although the upwash flow dominates the near wake region of the prisms (see Figure 14b,d). These rotational flow transforms into a pair of streamwise vortical structures within 3.85 h from the prism, which quickly grow to the same size as the prism height within 8 h downstream (Figure 20d). These streamwise vortices appear steady and with minimal diffusion far into the wake, $x/h \geq 20$ in Figure 20f.
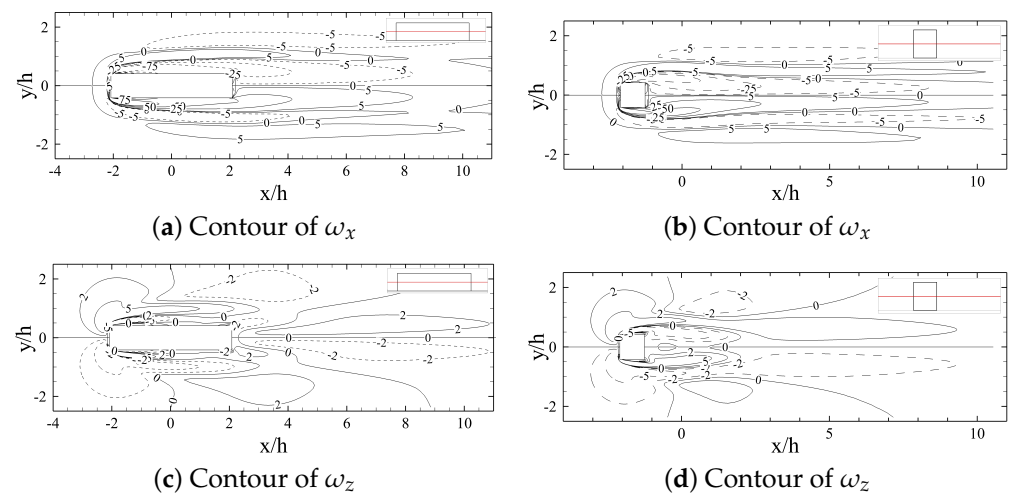

(**a**) Contour of ω_x

(**b**) Contour of ω_x

(**c**) Contour of ω_z

(**d**) Contour of ω_z

Figure 19. The contours of vorticity at the mid-height plane of the (**a**,**b**) long-rectangular prism and (**c**,**d**) square prism. The dotted lines indicate negative vorticity.

Figure 21 shows the 2D streamlines on yz-planes at different streamwise locations in the wake of the square (short) prism. There is clearly a different streamwise vortex formation mechanism at the rear face of the square prism compared to the long prism (see Figures 20a and 21a). This is mainly due to the large streamline curvatures on the xz-plane that entrain the fluid into the wake and trailing structures. There are evidence of streamwise horseshoe vortical structures in the immediate wake of the square prism, which diffuse rather quickly within 1 h into the wake. The tip vortices in the near wake region are different (see Figures 20c,d and 21c,d). Downstream at $x/h \geq 10$, however, the tip vortices are very similar to those of the long prism, whereas the structures are relatively smaller in the wake of the square prism. The main wake characteristics remain similar for both prisms, i.e., wake symmetry and steadiness.
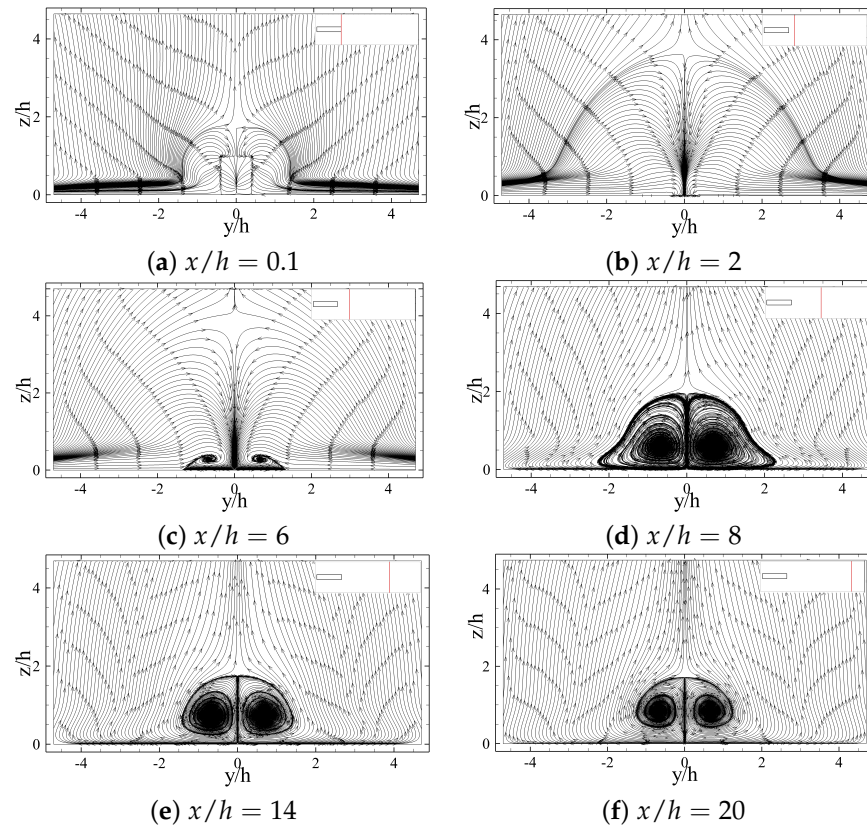
Figure 20. Mean streamlines on *zy*-planes at in the wake of the long prism.

Figure 22a,c shows two-dimensional streamlines on *yz*-planes at different streamwise locations along the long prism prior to the wake. These results reveal the formation of a pair of vortex structures on the contact lines of the upper and side faces close to the leading edge of the long prism. This structure vanishes before reaching the rear of the prism. These structures are not formed on the side faces and close to the leading edge of the square prism (Figure 22b,d), which are mainly due to the large streamline curvatures that form behind the square prism. There exists a similar structure in a very small region close to the rear face of the square prism, highlighted as S_1 and S_2 in Figure 22d, which does not extend into the wake region. The absence of these vortical structures in the near wake region of the two prisms hinted that these structures are not part of the wake tip vortices, although their sense of rotation is similar to tip vortices.

The differences in the wake of short and long prisms are also apparent from the velocity profiles at different streamwise locations in the wake, as shown in Figure 23. In the immediate wake, the two prisms exhibit different flow topologies with the square prism wake exhibiting a downwash flow that is reversed by mid-plane of the prism. There is also a second flow reversal at the tip of the prism. However, there is only one large upwash flow observed behind the long prism corresponding to the main structure that formed in the wake. It is also important to note that the velocity in the wake of the long prism tends towards zero after ≈1 h from the top face of the prism, whereas the shorter prism wake retains the upwash flow past 2 h above the top face of the prism. However, the velocity profile variations are similar in the far wake region of the two prisms. It is also notable that because of the stronger upwash flow in the wake of the square prism, there is a large magnitude of normal velocity compared to the long prism. Changing the velocity distribution alters the heat and mass transfer, which provides critical information that is useful in the engineering design of small heat sinks, cooling of electronic chips and flow manipulators for biomedical purposes.
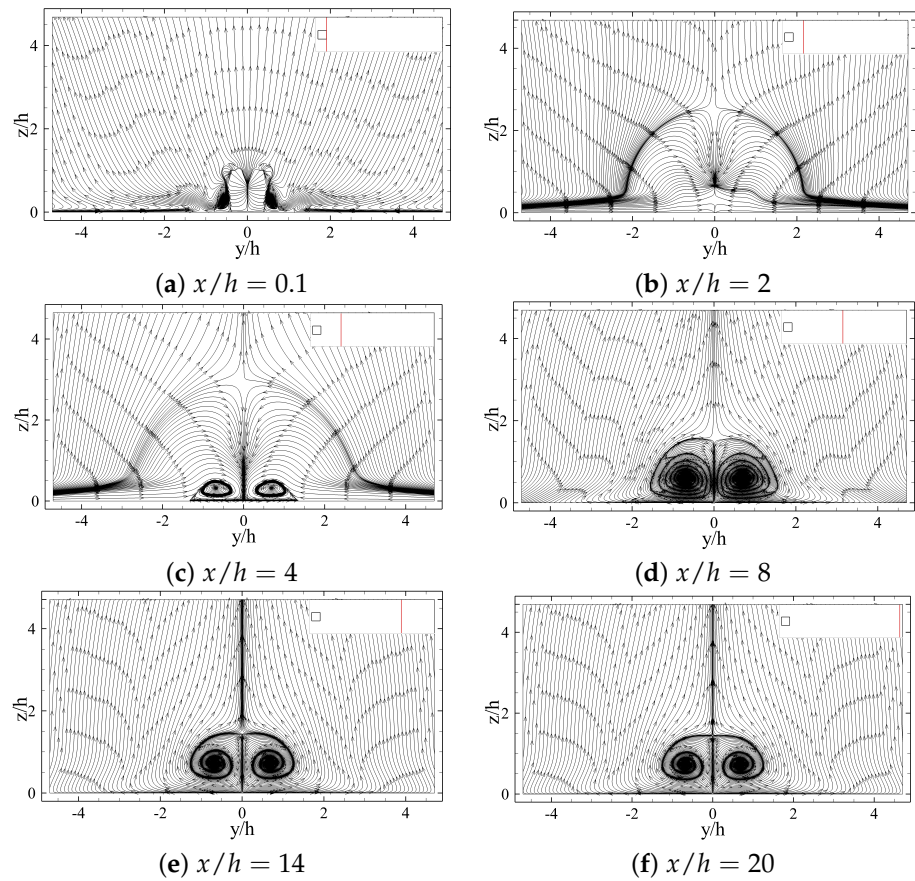
Figure 21. Mean streamlines on cross-sectional (*yz*-) planes at different distances from the square prism.
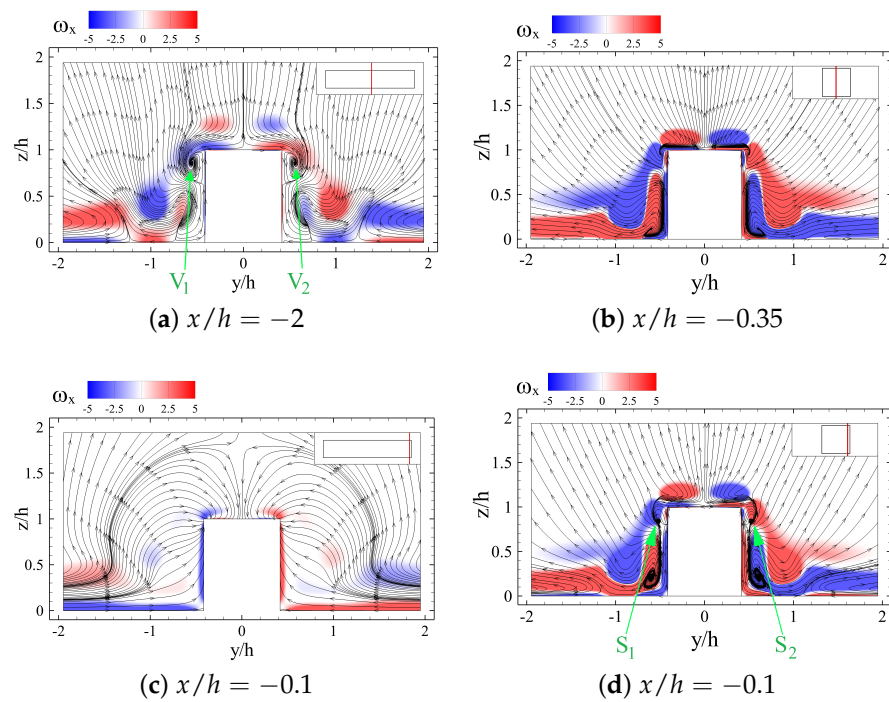

Figure 22. Mean streamlines on cross-sectional (*yz*-) planes along the (**a,c**) long and (**b,d**) square prisms.
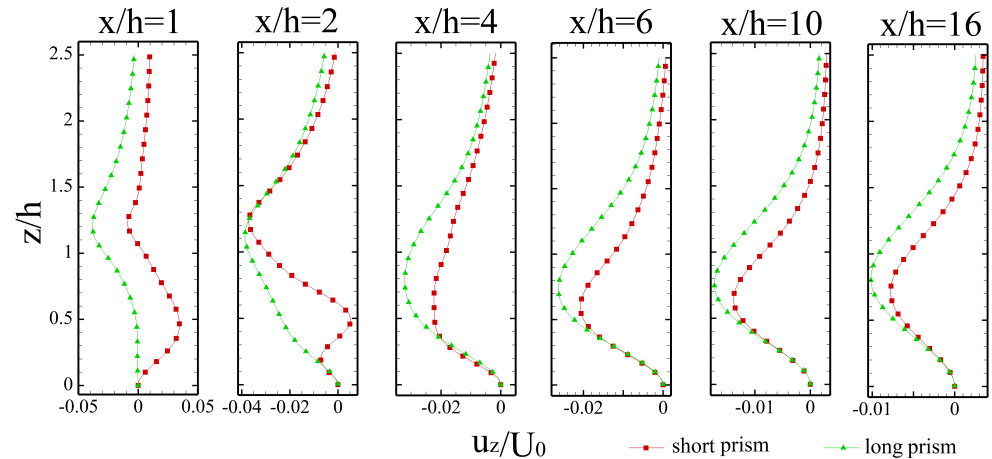
Figure 23. The profiles of spanwise velocity (u_z) in the symmetry plane of both prisms at different distances (identified as '*d*') from the rear face of the prism at $Re = 250$.

3.1. Reynolds Number Effect

The effect of the Reynolds number is examined by repeating the same analysis for $Re = 50$–200. The results illustrate that the flow around a rectangular prism with depth-ratio of $l/h = 4.17$ and aspect ratio of $h/w = 1.2$ is steady in the entire range of Re considered here, which was expected. As shown in Figure 24, increasing the Reynolds number from 50 to 250 leads to a consistent change in size of the wake. The streamwise length of the recirculation region (mean wake) increased from 1 h for $Re = 50$ to 2.2 h for $Re = 250$ (see Figure 25). These results show that the wake size scales with $Re^{1/2}$, as shown in Figure 25. The increase in the wake size can be attributed to the alteration of the downwash and upwash flow. As shown in Figure 24, increasing the Reynolds number led to the enhancement of the strength of upwash flow and the weakening of the downwash flow.
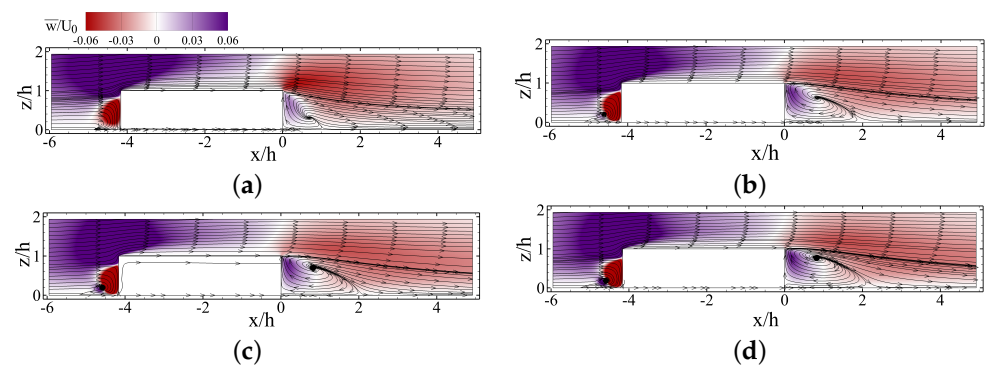

Figure 24. Streamlines on a side view (xz-) of the long prism ($DR = 4.17$) at $y/h = 0$ highlighted by the normal component of the velocity vector at $Re =$ (**a**) 50; (**b**) 150; (**c**) 200 and (**d**) 250.

Moreover, the location of the recirculation structure behind the prism moved away from the ground with increasing Re. Particularly, the focal point was located ~ 0.3 h above the ground at $Re = 50$, which moved to 0.65 h at $Re = 150$ and then settled at ~ 0.72 h for $Re \geq 200$. The streamwise location of the structure with respect to the rear face of the prism increased with Reynolds number in the range of $Re = 50$–150, but it was almost unchanged for $Re = 150$–250. In particular, the focal point was located at $x \sim 0.75$ h for $Re = 50$, which then moved to $x \sim 0.8$ h for $Re = 150$–250. It is notable that the shape of the wake structures remained unchanged in the range of low Reynolds number considered here (see Figure 26), although the strength of vortical structures changed due to variations in the strength of upwash and downwash flow. Therefore, establishing a constant flow skeleton model for this range is reasonable.
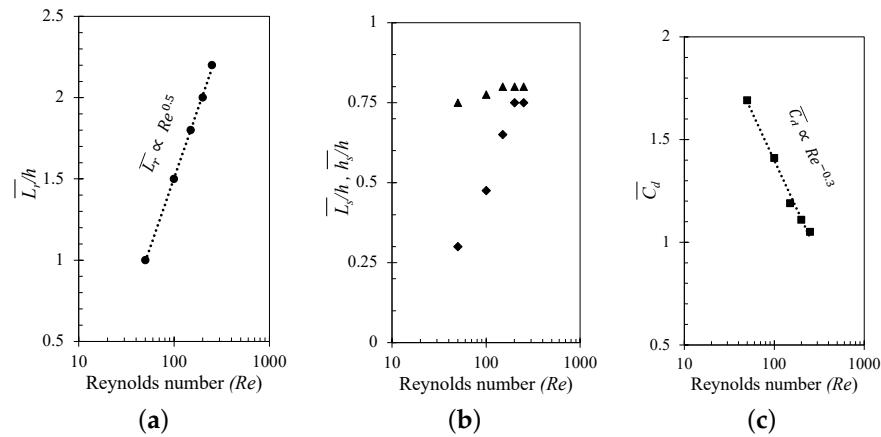
Figure 25. The variation of (**a**) wake size ($\overline{L_r}$ as ●), (**b**) height of the mean wake structure ($\overline{h_s}$ as ▲), and its distance from the rear face ($\overline{L_s}$ as ◆), and (**c**) mean drag coefficient ($\overline{C_d}$ as ■) at a range of *Re*.
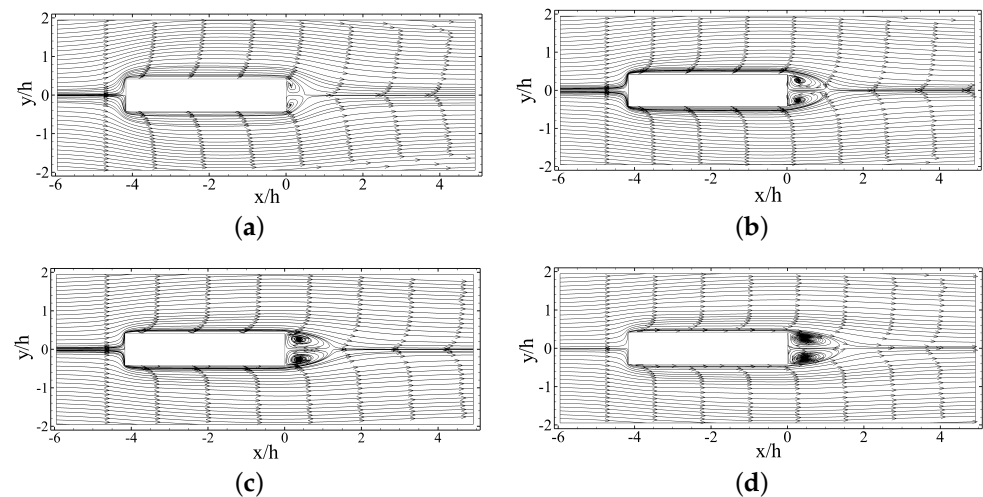

Figure 26. Streamlines on a top view (*xy*-) of the long prism ($DR = 4.17$) at $z/h = 0.5$. $Re = $ (**a**) 50; (**b**) 150; (**c**) 200 and (**d**) 250.

The drag coefficient of the prism is another parameter, which changes with respect to the Reynolds number. Similar to the drag coefficient of a sphere at low Reynolds numbers, the drag coefficient of the prism decreases from 1.69 at $Re = 50$ to 1.05 at $Re = 250$, which is depicted in Figure 25. The variations in drag appear to scale well with $Re^{-0.3}$.

3.2. Skeleton Model

The wake formed behind a long prism is evidently different from that identified and modeled for short prisms. Mainly, the direct contribution of the leading edge separated shear layer to the formation of the wake structures is prevented, and the wake is affected by the boundary layer formed on the long prism's upper and side faces. Thus, Figure 27 depicts the wake skeleton model for the case of flow around a long rectangular prism ($DR = 4.17$) at low Reynolds numbers ($50 \leq Re \leq 250$). This model is developed based on the observations made thus far, including the streamline and contour plots in various locations in the wake and the iso-surfaces of Q^* criterion. This model contains two Tip Vortices formed behind the body and the horseshoe vortex. The horseshoe vortex formed around the long prism appear to diffuse before reaching the wake, which coincides with the reattachment of the separated shear layer to the prism faces. This is different from the observations and models presented by da Silva et al. (2020) [7] and Wang et al. (2009 and 2004) [3,6], where the the horseshoe vortex and separated shear layer from the front face of a square prism fold into the wake region and form the wake structures. Moreover,

there exists a shear layer formed behind the body that separates from the topper edge of the prism and folds over its rear face. It generates a small region of upwash in the wake. However, the presence of two tip vortices induces a downwash flow in the wake. The next steps in this research involve determining the effects of Reynolds number in the wake unsteadiness and characterizing the unsteady wake at a higher Reynolds number.
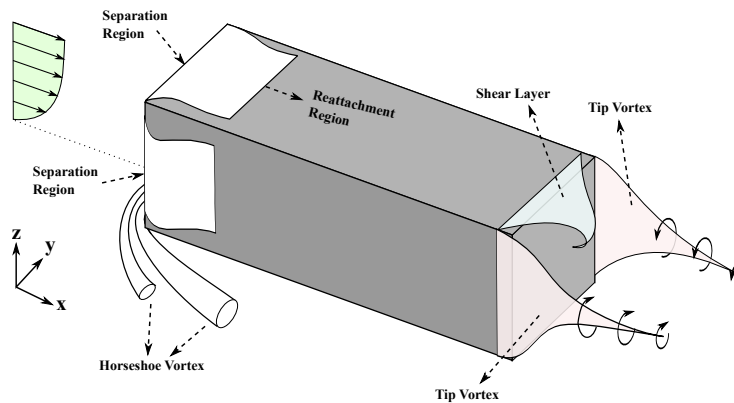

Figure 27. The skeleton model of the steady wake formed behind a long rectangular prism.

4. Conclusions

This study focused on fully characterizing the wake of a long prism at a low Reynolds number in an effort to fill the knowledge gap on the implications of depth ratio on wake topology. It was hypothesized that potential wake alternations originate from the reattachment of separated shear layer from the leading edges of the prism due to their elongated shape. The flow around two wall-mounted rectangular prisms with the depth-ratios of 0.83 and 4.17 are numerically studied at low Reynolds numbers ($50 \leq Re \leq 250$). The wakes are analyzed extensively for both shapes to identify changes in wake topology for the large depth-ratio (long) rectangular prism compared to a square prism. The wake descriptions identify significant variations in the wake topology between the two prisms, which are attributed to the larger depth-ratio of the long prism. The wake appears steady for both prisms due to the small aspect-ratio, which is consistent with existing observations. A skeleton model of the steady wake is proposed, which depicts the tip vortices and horseshoe vortex.

It is shown that the distributions of the critical points around the two prisms with different depth-ratios and the distribution of surface pressure coefficient on the rear faces are different. The strength of the upwash flow in the wake region of the square prism is higher than the long prism. This leads to different sizes of the recirculation region due to the large differences in their depth-ratios. Furthermore, the distribution of downwash flow from the tip region is different for the two cases.

As a result of flow entrainment from the leading edge separated shear layer, the streamwise structures of the near wake region are altered for the short prism. Moreover, there exist some streamwise structures close to the leading edge of the long prism that do not appear in the wake of the square prism. This difference is mainly attributed to the large streamline curvatures in front of the prism with a large-depth-ratio. However, a similar structure close to the trailing edge of the square prism is observed, where there is evidence of a large streamline curvature, larger vorticity magnitudes, and thus, more significant entrainment effects. This is mainly attributed to the smaller depth-ratio of the square prism, which facilitates the merge of structures in the rear and their interaction with the horseshoe structure. Horseshoe structures do not appear to interact with the wake for the long prism at low Reynolds numbers, which the flow behavior is steady.

There is an apparent effect of Reynolds number on the wake size for $Re = 50$–250 with a consistent increase in the wake size up to $Re = 150$ and the movement of the focal point away from the ground. The distance of the wake structure from the prism rear face scaled with $Re^{1/2}$, while the drag coefficient scaled with $Re^{-0.3}$.

References

1. Rastan, M.; Sohankar, A.; Alam, M.M. Low-Reynolds-number flow around a wall-mounted square cylinder: Flow structures and onset of vortex shedding. *Phys. Fluids* **2017**, *29*, 103601. [CrossRef]
2. Cimarelli, A.; Leonforte, A.; Angeli, D. Direct numerical simulation of the flow around a rectangular cylinder at a moderately high Reynolds number. *J. Wind Eng. Ind. Aerodyn.* **2018**, *174*, 39–49. [CrossRef]
3. Wang, H.; Zhou, Y. The finite-length square cylinder near wake. *J. Fluid Mech.* **2009**, *638*, 453–490. [CrossRef]
4. Taneda, S. An experimental study on the structure of the vortex street behind a circular cylinder of finite length. In *Research Report of Institute of Applied Mechanics*; Kyushu University: Fukuoka, Japan, 1952; Volume 1, pp. 131–142.
5. Sumner, D. Flow above the free end of a surface-mounted finite-height circular cylinder: A review. *J. Fluids Struct.* **2013**, *43*, 41–63. [CrossRef]
6. Wang, H.; Zhou, Y.; Chan, C.; Wong, W.; Lam, K. Flow structure around a finite-length square prism. In Proceedings of the 15 th Australasian Fluid Mechanics Conference, Sydney, Australia, 13–17 December 2004; pp. 13–17.
7. da Silva, B.L.; Chakravarty, R.; Sumner, D.; Bergstrom, D.J. Aerodynamic forces and three-dimensional flow structures in the mean wake of a surface-mounted finite-height square prism. *Int. J. Heat Fluid Flow* **2020**, *83*, 108569. [CrossRef]
8. Wei, Q.D.; Chen, G.; Du, X.D. An experimental study on the structure of juncture flows. *J. Vis.* **2001**, *3*, 341–348. [CrossRef]
9. Zhang, D.; Cheng, L.; An, H.; Zhao, M. Direct numerical simulation of flow around a surface-mounted finite square cylinder at low Reynolds numbers. *Phys. Fluids* **2017**, *29*, 045101. [CrossRef]
10. Uffinger, T.; Ali, I.; Becker, S. Experimental and numerical investigations of the flow around three different wall-mounted cylinder geometries of finite length. *J. Wind Eng. Ind. Aerodyn.* **2013**, *119*, 13–27. [CrossRef]
11. Sattari, P.; Bourgeois, J.; Martinuzzi, R. On the vortex dynamics in the wake of a finite surface-mounted square cylinder. *Exp. Fluids* **2012**, *52*, 1149–1167. [CrossRef]
12. Joubert, E.; Harms, T.; Venter, G. Computational simulation of the turbulent flow around a surface mounted rectangular prism. *J. Wind Eng. Ind. Aerodyn.* **2015**, *142*, 173–187. [CrossRef]
13. Lim, H.C.; Ohba, M. Detached eddy simulation of flow around rectangular bodies with different aspect ratios. *Wind Struct.* **2015**, *20*, 37–58. [CrossRef]
14. Wang, F.; Lam, K.M. Geometry effects on mean wake topology and large-scale coherent structures of wall-mounted prisms. *Phys. Fluids* **2019**, *31*, 125109. [CrossRef]
15. Saha, A.K. Unsteady flow past a finite square cylinder mounted on a wall at low Reynolds number. *Comput. Fluids* **2013**, *88*, 599–615. [CrossRef]
16. Sumner, D.; Rostamy, N.; Bergstrom, D.; Bugg, J. Influence of aspect ratio on the mean flow field of a surface-mounted finite-height square prism. *Int. J. Heat Fluid Flow* **2017**, *65*, 1–20. [CrossRef]
17. Rastan, M.; Sohankar, A.; Doolan, C.; Moreau, D.; Shirani, E.; Alam, M.M. Controlled flow over a finite square cylinder using suction and blowing. *Int. J. Mech. Sci.* **2019**, *156*, 410–434. [CrossRef]
18. Hosseini, Z.; Bourgeois, J.; Martinuzzi, R. Large-scale structures in dipole and quadrupole wakes of a wall-mounted finite rectangular cylinder. *Exp. Fluids* **2013**, *54*, 1595. [CrossRef]
19. El Hassan, M.; Bourgeois, J.; Martinuzzi, R. Boundary layer effect on the vortex shedding of wall-mounted rectangular cylinder. *Exp. Fluids* **2015**, *56*, 33. [CrossRef]
20. McClean, J.; Sumner, D. An experimental investigation of aspect ratio and incidence angle effects for the flow around surface-mounted finite-height square prisms. *J. Fluids Eng.* **2014**, *136*, 081206. [CrossRef]
21. Behera, S.; Saha, A.K. Characteristics of the Flow Past a Wall-Mounted Finite-Length Square Cylinder at Low Reynolds Number With Varying Boundary Layer Thickness. *J. Fluids Eng.* **2019**, *141*. [CrossRef]

22. Zhou, Q.; Cao, S.; Zhou, Z. Numerical studies on non-shear and shear flows past a 5:1 rectangular cylinder. *Wind Struct.* **2013**, *17*, 379–397. [CrossRef]

23. Jia, Y. The Implications of Coarctation and Indentation of the Aorta on Blood Flow Characteristics in Pediatric Patients. Master's Thesis, University of Alberta, Edmonton, Alberta, 2020.

24. Okajima, A.; Ueno, H.; Sakai, H. Numerical simulation of laminar and turbulent flows around rectangular cylinders. *Int. J. Numer. Methods Fluids* **1992**, *15*, 999–1012. [CrossRef]

25. Durbin, P.A.; Reif, B.P. *Statistical Theory and Modeling for Turbulent Flows*; John Wiley & Sons: Hoboken, NJ, USA, 2011.

26. Hemmati, A.; Wood, D.H.; Martinuzzi, R.J. On simulating the flow past a normal thin flat plate. *J. Wind Eng. Ind. Aerodyn.* **2018**, *174*, 170–187. [CrossRef]

27. Shah, K.B.; Ferziger, J.H. A fluid mechanicians view of wind engineering: Large eddy simulation of flow past a cubic obstacle. *J. Wind Eng. Ind. Aerodyn.* **1997**, *67*, 211–224. [CrossRef]

28. Krajnovic, S.; Davidson, L. Large-eddy simulation of the flow around a surface-mounted cube using a dynamic one-equation subgrid model. In *First Symposium on Turbulence and Shear Flow Phenomena*; Begel House Inc.: New York, NY, USA, 1999.

29. Yakhot, A.; Liu, H.; Nikitin, N. Turbulent flow around a wall-mounted cube: A direct numerical simulation. *Int. J. Heat Fluid Flow* **2006**, *27*, 994–1009. [CrossRef]

30. Krajnovic, S.; Davidson, L. Flow around a simplified car, part 1: Large eddy simulation. *J. Fluids Eng.* **2005**, *127*, 907–918. [CrossRef]

31. Krajnovic, S.; Davidson, L. Flow around a simplified car, part 2: Understanding the flow. *J. Fluids Eng.* **2005**, *127*, 919–928. [CrossRef]

32. Zargar, A.; Gongur, A.; Tarokh, A.; Hemmati, A. Coherent structures in the wake of a long wall-mounted rectangular cylinder at large incident angles. *J. Phys. Rev. Fluids* **2020**, *6*, 034603. [CrossRef]

33. Sohankar, A. Flow over a bluff body from moderate to high Reynolds numbers using large eddy simulation. *Comput. Fluids* **2006**, *35*, 1154–1168. [CrossRef]

34. Tobak, M.; Peake, D.J. Topology of three-dimensional separated flows. *Annu. Rev. Fluid Mech.* **1982**, *14*, 61–85. [CrossRef]

35. Chapman, G.T.; Yates, L.A. Topology of flow separation on three-dimensional bodies. *Appl. Mech. Rev.* **1991**, *44*, 329–345. [CrossRef]

36. Délery, J. *Three-Dimensional Separated Flow Topology: Critical Points, Separation Lines and Vortical Structures*; John Wiley & Sons: Hoboken, NJ, USA, 2013.

37. Liakos, A.; Malamataris, N.A. Direct numerical simulation of steady state, three dimensional, laminar flow around a wall mounted cube. *Phys. Fluids* **2014**, *26*, 053603. [CrossRef]

38. Hemmati, A.; Wood, D.H.; Martinuzzi, R.J. Characteristics of distinct flow regimes in the wake of an infinite span normal thin flat plate. *Int. J. Heat Fluid Flow* **2016**, *62*, 423–436. [CrossRef]